

SPTLC1 variants associated with ALS produce distinct sphingolipid signatures through impaired interaction with ORMDL proteins

Museer A. Lone, ... , Eric A. Shoubridge, Thorsten Hornemann

J Clin Invest. 2022;132(18):e161908. <https://doi.org/10.1172/JCI161908>.

Research Article

Neuroscience

Amyotrophic lateral sclerosis (ALS) is a progressive neurodegenerative disease that affects motor neurons. Mutations in the *SPTLC1* subunit of serine palmitoyltransferase (SPT), which catalyzes the first step in the de novo synthesis of sphingolipids (SLs), cause childhood-onset ALS. SPTLC1-ALS variants map to a transmembrane domain that interacts with ORMDL proteins, negative regulators of SPT activity. We show that ORMDL binding to the holoenzyme complex is impaired in cells expressing pathogenic SPTLC1-ALS alleles, resulting in increased SL synthesis and a distinct lipid signature. C-terminal SPTLC1 variants cause peripheral hereditary sensory and autonomic neuropathy type 1 (HSAN1) due to the synthesis of 1-deoxysphingolipids (1-deoxySLs) that form when SPT metabolizes L-alanine instead of L-serine. Limiting L-serine availability in SPTLC1-ALS-expressing cells increased 1-deoxySL and shifted the SL profile from an ALS to an HSAN1-like signature. This effect was corroborated in an SPTLC1-ALS pedigree in which the index patient uniquely presented with an HSAN1 phenotype, increased 1-deoxySL levels, and an L-serine deficiency. These data demonstrate how pathogenic variants in different domains of SPTLC1 give rise to distinct clinical presentations that are nonetheless modifiable by substrate availability.

Find the latest version:

<https://jci.me/161908/pdf>



SPTLC1 variants associated with ALS produce distinct sphingolipid signatures through impaired interaction with ORMDL proteins

Museer A. Lone,¹ Mari J. Aaltonen,^{2,3} Aliza Zidell,⁴ Helio F. Pedro,^{4,5} Jonas A. Morales Saute,^{6,7} Shalett Mathew,¹ Payam Mohassel,⁸ Carsten G. Bönnemann,⁸ Eric A. Shoubridge,^{2,3} and Thorsten Hornemann¹

¹Institute of Clinical Chemistry, University Hospital Zurich, University of Zurich, Zurich, Switzerland. ²Montreal Neurological Institute and ³Department of Human Genetics, McGill University, Montreal, Canada. ⁴Center for Genetic and Genomic Medicine, Hackensack University Medical Center, Hackensack, New Jersey, USA. ⁵Center for Genetic and Genomic Medicine, Hackensack University Medical Center, Hackensack Meridian School of Medicine, Hackensack, New Jersey, USA. ⁶Medical Genetics Division and Neurology Division, Hospital de Clinicas de Porto Alegre, Porto Alegre, Brazil. ⁷Graduate Program in Medicine, Medical Sciences, and Internal Medicine Department, Faculdade de Medicina, Universidade Federal do Rio Grande do Sul, Porto Alegre, Brazil. ⁸Neuromuscular and Neurogenetic Disorders of Childhood Section, National Institute of Neurological Disorders and Stroke, NIH, Bethesda, Maryland, USA.

Amyotrophic lateral sclerosis (ALS) is a progressive neurodegenerative disease that affects motor neurons. Mutations in the SPTLC1 subunit of serine palmitoyltransferase (SPT), which catalyzes the first step in the de novo synthesis of sphingolipids (SLs), cause childhood-onset ALS. SPTLC1-ALS variants map to a transmembrane domain that interacts with ORMDL proteins, negative regulators of SPT activity. We show that ORMDL binding to the holoenzyme complex is impaired in cells expressing pathogenic SPTLC1-ALS alleles, resulting in increased SL synthesis and a distinct lipid signature. C-terminal SPTLC1 variants cause peripheral hereditary sensory and autonomic neuropathy type 1 (HSAN1) due to the synthesis of 1-deoxysphingolipids (1-deoxySLs) that form when SPT metabolizes L-alanine instead of L-serine. Limiting L-serine availability in SPTLC1-ALS-expressing cells increased 1-deoxySL and shifted the SL profile from an ALS to an HSAN1-like signature. This effect was corroborated in an SPTLC1-ALS pedigree in which the index patient uniquely presented with an HSAN1 phenotype, increased 1-deoxySL levels, and an L-serine deficiency. These data demonstrate how pathogenic variants in different domains of SPTLC1 give rise to distinct clinical presentations that are nonetheless modifiable by substrate availability.

Introduction

Amyotrophic lateral sclerosis (ALS) is a progressive, neurodegenerative disease of the lower and upper motor neurons characterized by severe muscle wasting, eventually leading to paralysis and death (1, 2). Approximately 90% of the ALS cases are sporadic, frequently without a recognized heritable factor, while an increasing number of genetic causes account for about 10% of ALS cases with a familial background, and a number of those without a clear family history (3).

Recently, dominant de novo missense and deletion mutations in *SPTLC1* were associated with childhood-onset ALS (4–6). *SPTLC1* and *SPTLC2* are essential subunits of the enzyme serine palmitoyltransferase (SPT), which catalyzes the first and rate-limiting step in the de novo synthesis of sphingolipids (SLs) (Supplemental Figure 1A; supplemental material available online with this article; <https://doi.org/10.1172/JCI161908DS1>). SPT typically conjugates palmitoyl-CoA with L-serine in a pyridoxal 5-phosphate-dependent reaction but it can also metabolize L-alanine and

glycine under certain conditions, forming an atypical class of toxic 1-deoxysphingolipids (1-deoxySLs) that cannot be metabolized to complex SLs or degraded by canonical SL catabolism (7). Variants in the cytoplasmic domains of *SPTLC1* and *SPTLC2* result in pathologically increased 1-deoxySL levels, causing hereditary sensory and autonomic neuropathy type 1 (HSAN1) (8, 9), an autosomal dominant axonopathy characterized by a progressive sensory loss with variable autonomic involvement (10–13). Although the majority of reported *SPTLC1*-HSAN1 variants are associated with sensory symptoms, a significant motor involvement was reported for the 2 variants, *SPTLC1*-S331F and *SPTLC1*-S331Y (14). The SPT enzyme complex resides in the endoplasmic reticulum (ER) membrane and at the ER-mitochondria contact sites (15). SPT is typically composed of 2 *SPTLC1*-*SPTLC2* dimers that interact with the accessory subunits ssSPTa/b and the regulatory ORMDL proteins ORMDL1, -2, and -3, which are paralogous and functionally redundant proteins (16, 17). ORMDLs interact with the N-terminal transmembrane domain (TMD) of *SPTLC1* and act as lipid sensors negatively regulating SPT activity (18–20). All reported *SPTLC1*-ALS missense variants reside within this TMD (Figure 1A and Supplemental Figure 1B) and one causes an in-frame splice skip of exon 2 that results in a form of *SPTLC1* protein completely lacking this TMD (4). Our previous results showed that *SPTLC1*-ALS variants caused an unregulated synthesis of SLs that did not respond to increasing concentrations of ORMDL3 in an in vitro

Authorship note: MAL and MJA contributed equally to this work.

Conflict of interest: The authors have declared that no conflict of interest exists.

Copyright: © 2022, Lone et al. This is an open access article published under the terms of the Creative Commons Attribution 4.0 International License.

Submitted: May 23, 2022; **Accepted:** July 26, 2022; **Published:** September 15, 2022.

Reference information: *J Clin Invest.* 2022;132(18):e161908.

<https://doi.org/10.1172/JCI161908>.

assay, suggesting that the pathogenic variants could prevent the association of ORMDL proteins with the holoenzyme complex.

Here we have expanded the analysis of SPTLC1 variants, tested whether the variants impair the association of ORMDLs with the SPT complex, defined distinct lipid signatures associated with the expression of SPTLC1-ALS and -HSAN1 alleles, and investigated the influence of altered substrate availability on the lipid signatures and clinical phenotypes caused by mutations in different domains of SPTLC1.

Results

Loss of exon 2 in SPTLC1 impairs integration into the ER membrane. SPTLC1 is an ER-localized protein with an N-terminal TMD (Figure 1A and Supplemental Figure 1B). The amino acids in the TMD could be important for the interaction with ORMDL proteins, but as they could also be essential for ER targeting and membrane integration of SPTLC1, we first set out to determine the localization and membrane association of a subset of pathogenic SPTLC1 variants in detail, namely the ALS variants Y23F, L39del, F40S41del, a variant missing the whole of exon 2 (ex2del) induced by aberrant splicing in an A20S patient (4), and the HSAN1 variants C133W and S331F (Figure 1A). C-terminally FLAG-tagged SPTLC1 was colocalized with the ER marker Sec61b-mCherry by confocal microscopy when expressed transiently in COS-7 cells, and ER localization was observed for all variants (C133W, S331F, Y23F, L39del, and F40S41del) except for the ex2del variant, which lacks the entire TMD and showed a mostly cytosolic distribution when expressed transiently (Figure 1B).

For the biochemical analysis of SPTLC1 variants, C-terminally FLAG-tagged WT SPTLC1 and the C133W, S331F, Y23F, L39del, F40S41del, and ex2del variants were integrated into Flp-In T-Rex 293 SPTLC1-KO cells (Figure 1C). The stability of SPTLC2 depends on SPTLC1 (15, 21) and the diminished level of SPTLC2 in SPTLC1-KO cells (17% of control) was rescued upon reexpression of WT, C133W, S331F, and Y23F variants, while a partial rescue was observed with the L39del (77% of control), F40S41del (68% of control), and ex2del (38% of control) variants (Figure 1, C and D).

Considering that the ex2del variant partially rescues SPTLC2 protein levels, we hypothesized that a fraction of this variant might still be associated with SPTLC2 at the ER and mitochondrial membranes that could have been masked in the microscopy analysis due to a high expression of transiently transfected constructs. To further analyze the membrane association of SPTLC1 and variants, membranes and cytosol were separated by ultracentrifugation from Flp-In T-Rex 293 control cells and variant-expressing SPTLC1-KO cells. Endogenous SPTLC1 and WT-SPTLC1^{FLAG} were found in the membrane pellet, as was the ER membrane protein VAPB, while the cytosolic protein UBB was in the supernatant (Figure 1E). All variants were predominantly detected in the membrane pellet fraction, except for the ex2del variant which was enriched in the cytosolic supernatant (Figure 1E). However, part of the ex2del variant was present in the membrane pellet, suggesting that a portion of it was still associated with membranes, likely through interaction of the SPTLC1 aminotransferase domain with SPTLC2.

In summary, neither the HSAN1- or the ALS-causing mutations in SPTLC1 impair the ER localization and membrane association of the protein, except for the TMD-lacking ex2del variant which is predominantly soluble in the cytosol and only partially associated with membranes.

ORMDLs fail to interact with SPTLC1 variants. The patient mutations in SPTLC1 could impair the interaction of SPTLC1 with ORMDLs, as structural studies have shown that amino acids in the TMD interact with one of the ORMDL-TMDs, and some amino acids close to the catalytic site, such as SPTLC1-S331, interact with the N-terminal loop of ORMDLs that can reach into the active site to occupy the substrate-binding tunnel (16). To analyze the interaction of pathogenic SPTLC1 variants with SPTLC2 and ORMDLs, FLAG-tagged SPTLC1 and variants were purified by FLAG immunoprecipitation from digitonin-solubilized membrane fractions, and input and eluate fractions were analyzed by immunoblotting. Similar amounts of SPTLC2 copurified with all variants except the ex2del variant, which showed a reduced interaction (Figure 2A). However, the level of ex2del variant was lower in the membrane fraction input, as a majority of the protein is cytosolic, and these cells also have less SPTLC2 (Figure 1, B–D). Immunoblotting with a pan ORMDL antibody that detects all isoforms (22) showed that the interaction with ORMDLs was completely abolished by the ex2del variant, which lacks the whole TMD (Figure 2A). The other variants affecting the SPTLC1 TMD, L39del and F40S41del, showed a diminished interaction with ORMDLs, while Y23F retained interaction with ORMDLs (Figure 2A). The variants with mutations in the active site, C133W and S331F, showed a reduced interaction with ORMDLs (Figure 2A).

Next, we asked whether the interaction of ORMDLs with the SPT complex could be detected on a native gel where protein-protein interactions within a protein complex are preserved. The separation of digitonin-solubilized membrane fractions on a native gel, followed by immunoblotting with anti-SPTLC1, -SPTLC2, and -ORMDL antibodies, showed that ORMDLs migrated together with SPTLC1 and SPTLC2 in a complex of roughly 350–400 kDa (Figure 2B). This complex was completely absent in SPTLC1- or SPTLC2-KO cells (Figure 2B), while ORMDL proteins could still be detected on a denaturing gel, although at lower levels compared with control (Supplemental Figure 2A). Notably, the levels of ORMDLs were reduced in SPTLC1-KO (40% of control) and SPTLC2-KO (49% of control) cells (Supplemental Figure 2, B and C).

To investigate the formation of the SPT complex upon expression of the pathogenic variants, isolated membrane fractions were analyzed on a native gel. Expression of WT-SPTLC1^{FLAG} in SPTLC1-KO cells rescued the formation of the SPT complex, as SPTLC1, SPTLC2, and ORMDLs could be detected in a complex, although at a slightly higher molecular weight than in control due to the epitope tag (Figure 2C). In SPTLC1-KO cells expressing the S331F, L39del, F40S41del, and ex2del variants, the full-size SPT complex was disassembled, as ORMDLs were absent from the complex (Figure 2C), while ORMDLs could still be detected in these samples on a denaturing gel (Supplemental Figure 2D). Instead, the S331F, L39del, and F40S41del SPTLC1 variants formed slightly lower molecular weight complexes with SPTLC2 that were devoid of ORMDLs, and the ex2del variant only allowed the assembly of an approximately 140 kDa SPTLC1-SPTLC2 complex, suggesting that loss of exon 2 also interferes with oligomerization of SPTLC1-SPTLC2 heterodimers (Figure 2C). SPTLC1, SPTLC2, and ORMDLs could still be detected in the full SPT complex with the Y23F and C133W variants, although C133W showed lower levels of this complex (Figure 2C). We observed a disassembly of the SPT complex also in S331Y and L39del patient fibroblasts, with reduced ORMDLs in the SPT complex and a shift

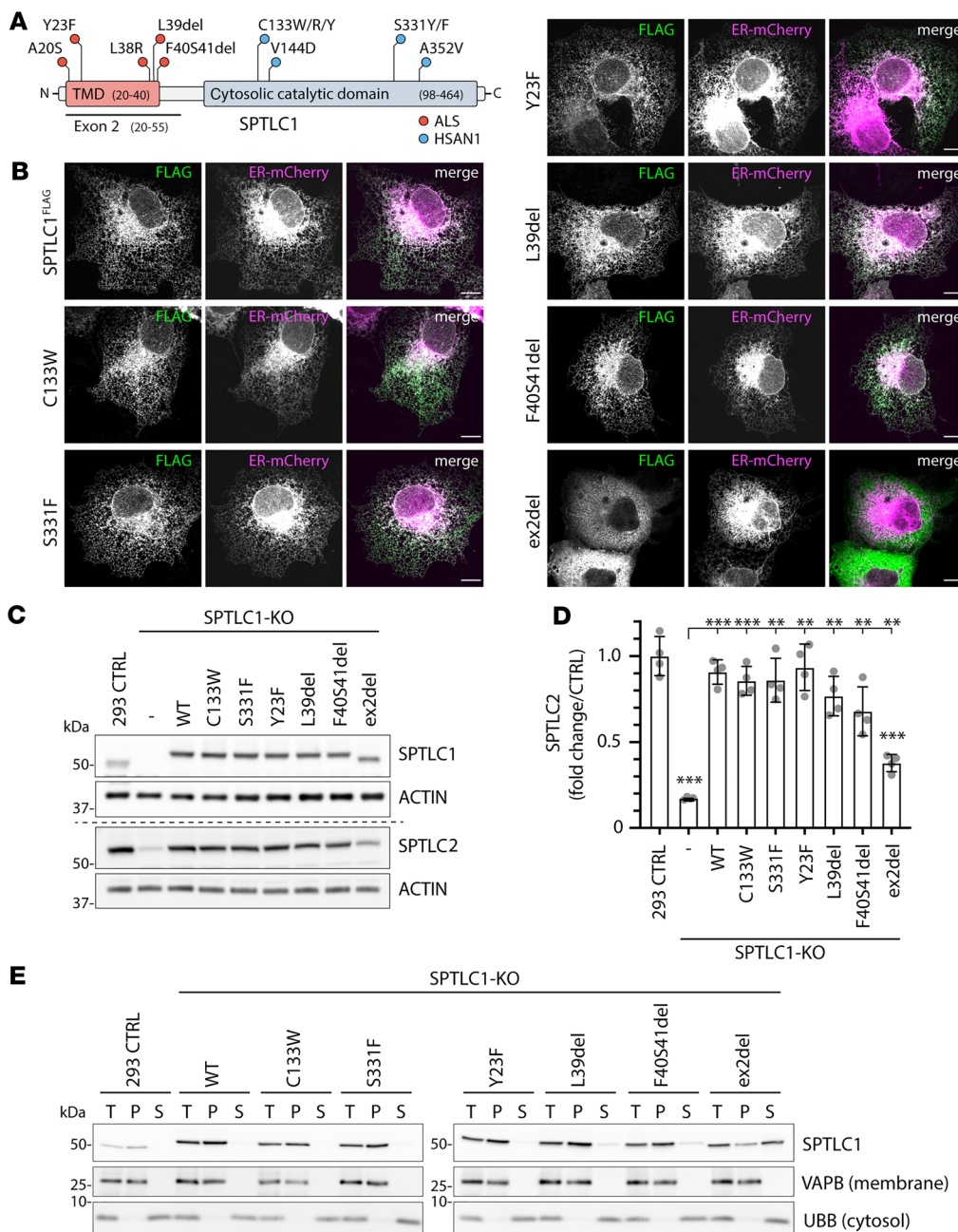


Figure 1. Localization and membrane association of SPTLC1 and pathogenic variants. (A) Schematic of SPTLC1 displaying individual protein domains and positions of ALS and HSNAN1 pathogenic variants. TMD, transmembrane domain. (B) Confocal images of SPTLC1 localization. WT-SPTLC1^{FLAG} and variants were transiently expressed in COS-7 cells and visualized using an anti-FLAG antibody. ER-mCherry serves as an ER marker. Scale bars: 10 μm. (C and D) Expression of SPTLC1 variants in SPTLC1-KO cells. WT-SPTLC1^{FLAG} and variants were integrated into Flp-In T-Rex 293 SPTLC1-KO cells and expressed by addition of tetracycline. Whole-cell lysates were analyzed by SDS-PAGE and immunoblotting with anti-SPTLC1 and anti-SPTLC2 antibodies (C), and SPTLC2 levels were quantified (D). SPTLC2 signals were normalized to the β-actin signal. Mean ± SD, n = 4 independent replicates, unpaired 2-sided Welch's *t* test. ***P* < 0.01, ****P* < 0.001. (E) Analysis of membrane association of SPTLC1 variants. Cell lysates from Flp-In T-Rex 293 control cells and SPTLC1-KO cells expressing WT-SPTLC1^{FLAG} and variants were centrifuged to separate the membrane pellet and cytosolic supernatant. Equal amounts of total (T), pellet (P), and supernatant (S) were analyzed by SDS-PAGE and immunoblotted for VAPB as a membrane protein control and UBB as a cytosolic protein control. See complete unedited blots for C and E in the supplemental material.

in SPTLC2, although the phenotype was not as dramatic as upon expression of variants in a KO background, likely due to patient cells having 1 WT allele (Supplemental Figure 2, E and F).

In conclusion, coimmunoprecipitation and native PAGE analyses show that pathogenic SPTLC1 variants S331F, L39del, F40S41del, and ex2del lose interaction with ORMDLs, leading to a shift in the size of the SPTLC1-SPTLC2 complex. The C133W variant also showed a reduced interaction with ORMDLs, while Y23F supported the interaction and holoenzyme complex assembly.

SPTLC1 variants show impaired regulation by ORMDLs. We next investigated the enzymatic properties of pathogenic SPTLC1 variants by analyzing de novo SL synthesis in HEK293 SPTLC1-KO cells expressing the pathogenic SPTLC1 variants. Cellular SPT activity was analyzed with a metabolic labeling assay in which cells

were grown in serine- and alanine-deficient medium supplemented with stable isotope-labeled D₃-¹⁵N-L-serine (to label canonical SL) and D₄-L-alanine (to label 1-deoxySL). For quantification, total SLs were extracted and quantified by high-resolution mass spectrometry. The interaction of ORMDLs with SPT inhibits SPT activity, as knockdown (Figure 2D) (23) or knockout (22) of all ORMDLs leads to increased SL synthesis. In contrast, while the expression of SPTLC1 variants L39del and ex2del in SPTLC1-KO cells led to an overall increase in SL synthesis compared with WT-SPTLC1-expressing cells, silencing ORMDLs had little or no effect on the activity of the L39del and ex2del variant (Figure 2E), suggesting that increased SL synthesis by the variants is primarily caused by dysfunctional feedback inhibition rather than by an increased activity of the holoenzyme.

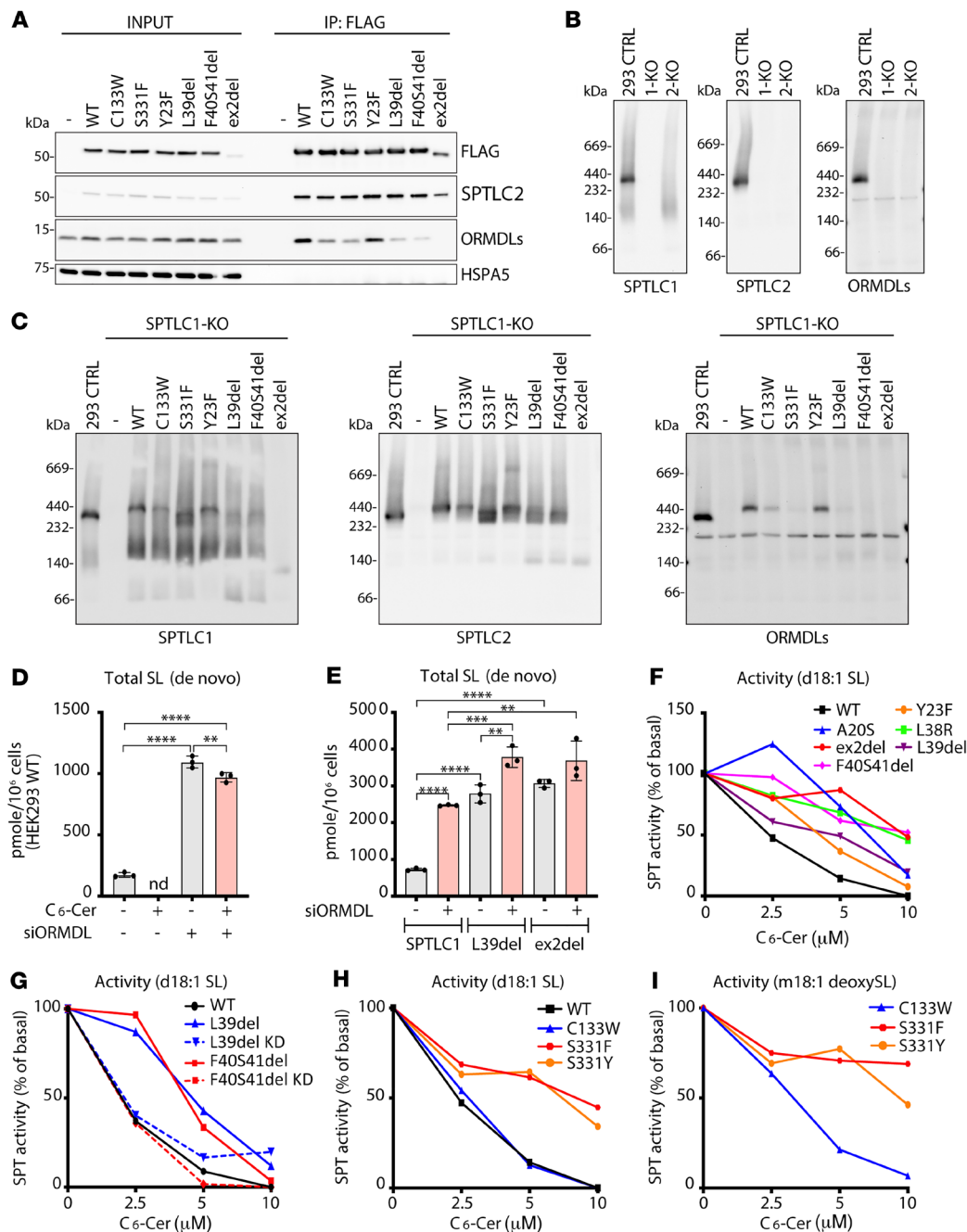


Figure 2. Interaction of SPTLC1 variants with ORMDLs. (A) Immunoblot analysis of proteins copurified with SPTLC1^{FLAG} variants. Membrane fractions from Flp-In T-REx 293 control cells and SPTLC1-KO cells expressing WT-SPTLC1^{FLAG} and variants were solubilized by digitonin and subjected to FLAG immunoprecipitation. Input (5%) and eluate (IP: anti-FLAG, 40%) fractions were analyzed by SDS-PAGE and immunoblotting. HSPA5 was used as a negative control. (B and C) Analysis of the SPT complex by blue native PAGE. Membrane fractions from Flp-In T-REx 293 control (CTRL), SPTLC1-KO, and SPTLC2-KO cells (B), or SPTLC1-KO cells expressing WT-SPTLC1^{FLAG} and variants (C) were analyzed by blue native PAGE and immunoblotted with anti-SPTLC1, anti-SPTLC2, and anti-ORMDL antibodies. See complete unedited blots for A–C in the supplemental material. (D) SPT activity in WT HEK293 cells after the siRNA-mediated silencing of ORMDL expression, in the presence or absence of C₆-ceramide (C₆-Cer). Cells were transfected with either nontargeting scrambled control or isoform-independent ORMDL siRNA. Isotope labeling using D₃-¹⁵N-L-serine was done 72 hours after transfection. De novo–formed sphingolipids (SLs) were quantified by the incorporation of isotope-labeled D₃-¹⁵N-L-serine. (E) SPT activity in SPTLC1-deficient HEK293 cells expressing WT SPTLC1 and the SPTLC1-ALS variants L39del and ex2del. Cells were transfected with either scrambled or ORMDL siRNAs. Seventy-two hours after transfection, cells were labeled with D₃-¹⁵N-L-serine (for 16 hours) and total de novo–formed SLs quantified by LC-MS. (F) SPT activity in WT- or ALS-variant-expressing SPTLC1-KO cells in response to the addition of C₆-Cer. Cells were grown with increasing concentrations of C₆-Cer. Each data point reflects a single measurement. (G) De novo SL formation in patient-derived primary fibroblasts carrying either the SPTLC1p.L39del or the F40S41del mutation. Control (WT) and mutant fibroblasts were transfected with scrambled or mutant allele-specific siRNA. SL de novo formation was measured in the presence of C₆-Cer. The plot shows the total amount of de novo–formed SLs relative to untreated controls. (H and I) Formation of canonical and 1-deoxySL in SPTLC1-KO cells expressing the HSAN1 variants SPTLC1, C133W, S331F, and S331Y. The plot shows total de novo–formed SLs (H) and 1-deoxySLs (I) at the given C₆-Cer concentration. SPT activity was measured by the incorporation of D₃-¹⁵N-L-serine and D₄-L-alanine. Mean ± SD, n = 3 independent replicates, 1-way ANOVA with Bonferroni's adjustment for multiple comparisons. **P < 0.01; ***P < 0.001; ****P < 0.0001.

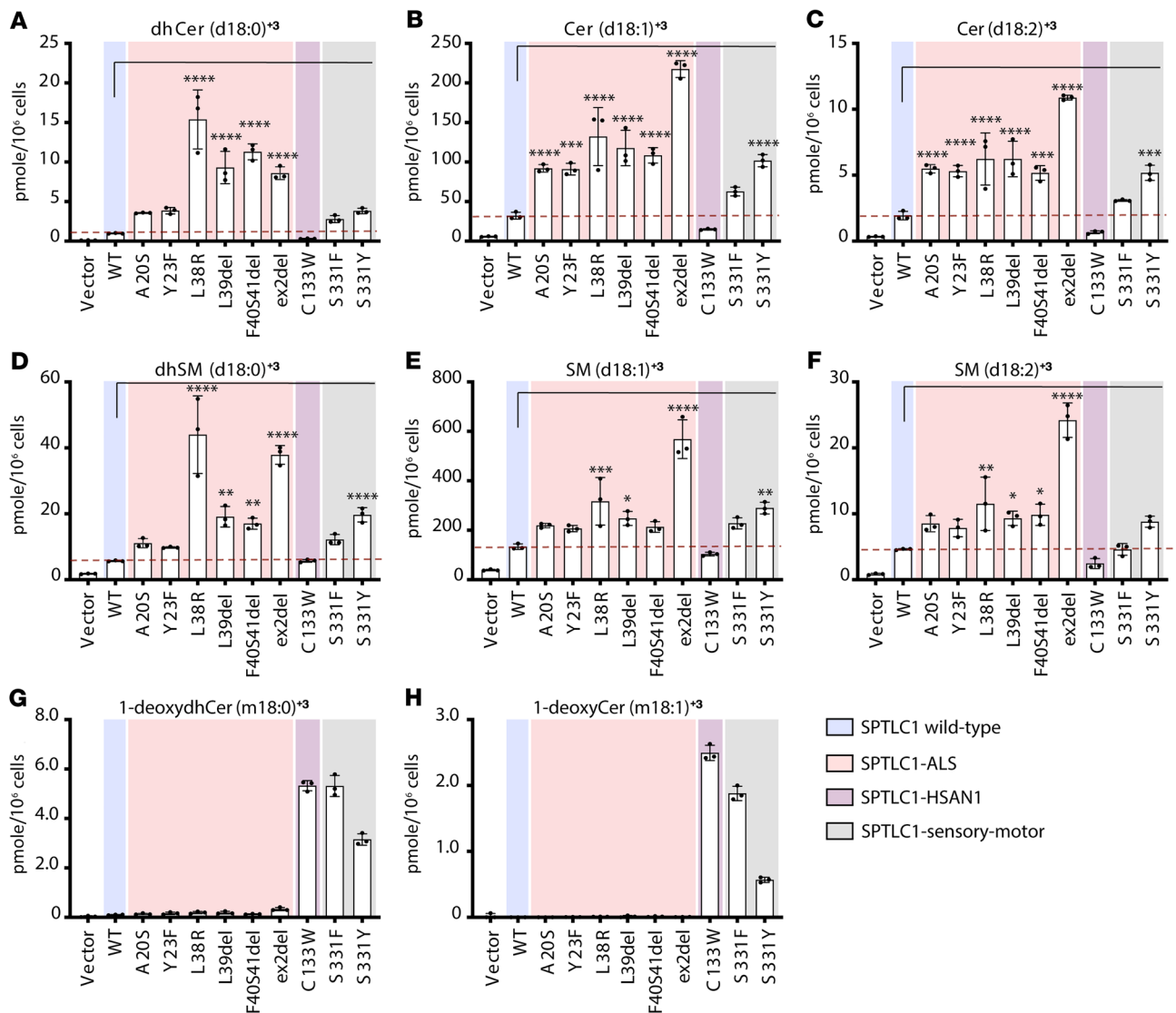


Figure 3. De novo sphingolipid (SL) synthesis in variant-expressing cells. (A–F) De novo formation of ceramides (Cer, A–C), sphingomyelins (SM, D–F), and 1-deoxyceramides (G and H) in HEK293 SPTLC1-KO cells expressing WT-SPTLC1 and variants. Cells were probed for de novo SPT activity by a stable isotope labeling assay that incorporates D_3 - ^{15}N -L-serine in SL and D_3 -L-alanine in 1-deoxySL, inducing a mass shift (+3 Da) in the respective de novo-formed SLs and absolute levels of each SL species were measured relative to an internal lipid standard. Data are represented as mean \pm SD, $n = 3$ independent replicates, 1-way ANOVA with Bonferroni's adjustment for multiple comparison. * $P < 0.05$, ** $P < 0.01$, *** $P < 0.001$, **** $P < 0.0001$.

ORMDLs play a role in homeostatic feedback regulation of SPT activity by ceramides (24), as addition of cell-permeant C_6 -ceramide (C_6 -Cer) inhibits SL synthesis, while the inhibitory effect is blunted in the absence of ORMDLs (Figure 2D) (23). In WT-SPTLC1-expressing cells, de novo SL synthesis was gradually reduced and ultimately suppressed with increasing concentrations of C_6 -Cer (Figure 2F). In contrast, SPTLC1 variants affecting the TMD showed a reduced response to inhibition of SL synthesis by C_6 -Cer, with the strongest effect seen for the L38R, F40S41del, and ex2del variants. An attenuated C_6 -Cer response was also observed in fibroblasts derived from L39del and F40S41del patients, which could be restored after knock-down of the mutant mRNA transcripts (Figure 2G) using siRNAs that specifically silence the expression of the respective mutant alleles, as shown previously (4). Additionally, the SL synthesis by variants S331F and S331Y was resistant to C_6 -Cer treatment, whereas the response

in the C133W-expressing cells was similar to WT (Figure 2H). C_6 -Cer-induced inhibition was also seen for synthesis of 1-deoxySL in C133W- but not in S331Y- and S331F-expressing cells (Figure 2I).

In summary, the lack of interaction of SPTLC1-ALS variants with the ORMDLs results in dysfunctional feedback regulation and increased SPT activity, leading to higher SL levels in cells.

Lipid signatures of motor and sensory neuropathy. To define and compare the distinct alterations in SL classes and species induced in SPTLC1-associated ALS and HSN1 disease conditions, we analyzed SL profiles in variant-expressing cells and patient-derived plasma and fibroblasts.

First, we expressed the variants in HEK293 SPTLC1-KO cells and quantified the labeled de novo-synthesized SL species, including ceramides, sphingomyelins (SMs), and 1-deoxyceramides. Compared with WT-SPTLC1-expressing cells, SPTLC1-ALS variants affecting

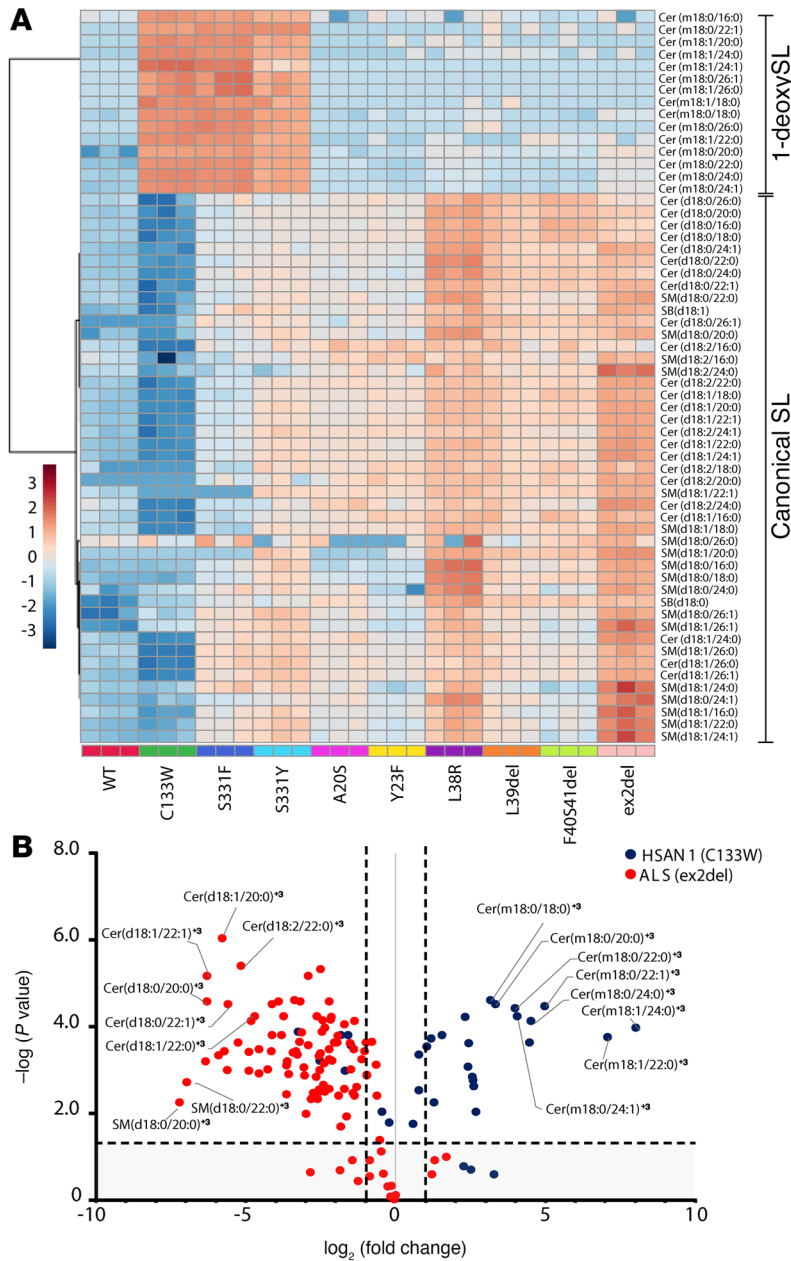


Figure 4. Sphingolipid (SL) signatures in variant-expressing cells. (A) Heatmap cluster analysis of de novo-formed SL species from HEK293 SPTLC1-KO cells expressing WT SPTLC1, SPTLC1-ALS, or SPTLC1-HSAN1 variants. Absolute levels of each SL species were measured relative to an internal lipid standard. Shown is a plot of the \log_{10} -transformed data with Euclidean distance measure. SB, sphingoid base. **(B)** Volcano plot comparing de novo-formed SL species in SPTLC1-KO cells expressing the SPTLC1-HSAN1 (C133W) and SPTLC1-ALS (ex2del) variants. MetaboAnalyst Suite 5.0 was used for comparison of species profiles as heatmaps and volcano plot. $n = 3$ independent biological replicates, significance (P) and fold change (FC) are represented as dotted lines.

the TMD (A2OS, Y23F, L38R, L39del, F40S41del, ex2del) showed an increased formation of canonical SLs, including those with saturated (d18:0), mono- (d18:1), and di-unsaturated (d18:2) sphingoid bases (Figure 3, A-F). The highest levels were measured for the ex2del variant, followed by the L38R, L39del, and F40S41del variants, while the A2OS and Y23F variants showed modest accumulations.

The HSAN1 variant C133W did not increase synthesis of canonical SLs but in contrast induced the formation of 1-deoxySLs (m18:0, m18:1), which were not formed by the TMD variants (Figure 3, G and H). The S331F and S331Y variants gave rise to a combined biochemical phenotype with increased synthesis of both canonical SLs and 1-deoxySLs.

A comparison of the plasma SL profile between the ALS patients carrying the Y23F, L39del, and F40S41del variants and unrelated HSAN1 patients carrying the C133W variant revealed similar changes in SL profiles, with increased SL levels in ALS patient plasma and higher 1-deoxyceramide levels in the HSAN1 patients (Supplemental Figure 3, A-D). There were, however, variations in the SL classes and species, as ceramides, SMs, and hexosyl-ceramides were differently affected in different patients, and the relative increases were more prominent for ceramides with saturated (d18:0) sphingoid bases compared with unsaturated (d18:1 or d18:2) backbones (Supplemental Figure 3, A-D).

To characterize the SL pattern associated with SPTLC1-ALS and -HSAN1 variants, we compared the profile of de novo-formed SL species between HEK293 SPTLC1-KO cells expressing the pathogenic SPTLC1 variants. A heatmap cluster analysis showed significant differences in the de novo-formed SL profiles (Figure 4A). The HSAN1 variants C133W, S331F, and S331Y clustered due to the increase in 1-deoxySL species, while the ALS TMD variants clustered due to the relative enrichment in canonical SL species. The S331 variants showed a mixed pattern that partly resembled the TMD variants due to increased synthesis of canonical SLs, with the S331F variant showing more similarity with the HSAN1 C133W variant, and S331Y with the ALS TMD variants (Figure 4A). The ex2del variant showed the strongest relative accumulation of canonical SL species, followed by the L38R, F40S41del, and L39del variants.

We next explored the changes in SL species in detail by volcano plot comparison of SL enrichment in cells expressing the HSAN1 variant C133W relative to those expressing the ALS variant ex2del. In addition to the prominent enrichment of de novo-formed 1-deoxyceramide species in C133W-expressing cells, in ex2del-expressing cells there was an enrichment of distinct ceramide species with uncommon N-acyl chains (Figure 4B). The most abundant ceramides in HEK293 cells carry fatty acids C_{16} , $C_{24:0}$, and $C_{24:1}$, while ceramides with $C_{18:0}$, $C_{20:0}$, $C_{22:0}$, and $C_{22:1}$ acyl chains, which have very low abundance in WT-expressing cells, accumulated in cells expressing ex2del (Figure 4B) and also in cells expressing other TMD and S331 variants (Supplemental Figure 4, A and B). The intermediate chain length ceramide species form only a small fraction of the total SLs in WT-SPTLC1-expressing cells, but an increased fraction in ex2del-expressing cells relative to total species, despite the overall higher SL amount

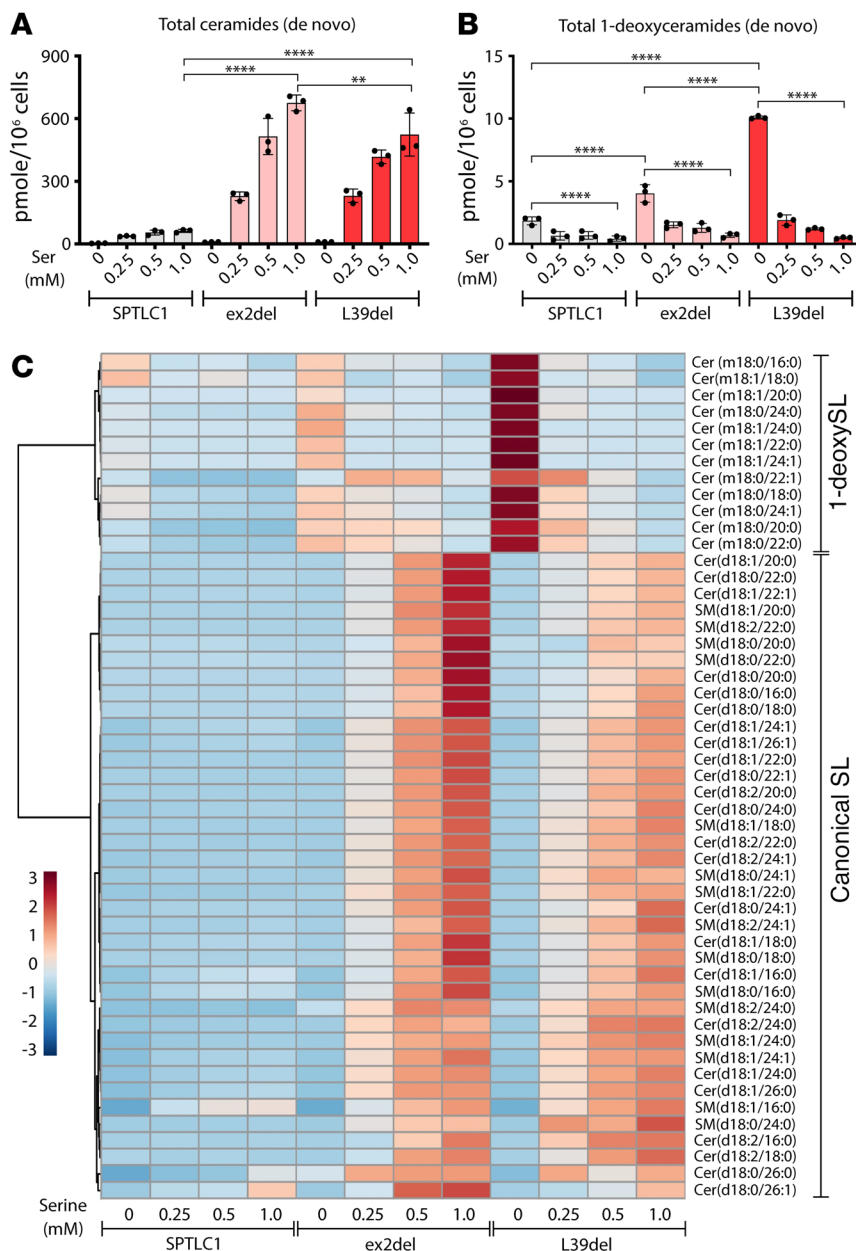


Figure 5. Sphingolipid (SL) signatures shift upon amino acid availability. (A and B) Total de novo-formed (A) ceramides and (B) 1-deoxyceramides in HEK293 SPTLC1-KO cells expressing SPTLC1 WT, ex2del, and L39del variants. Cells were treated with increasing D₃-¹⁵N-L-serine (0 to 1 mM) in the presence of a constant D₄-L-alanine concentration (2 mM). Data are represented as mean ± SD, n = 3 independent replicates, 1-way ANOVA with Bonferroni’s adjustment was used for pairwise comparison. **P < 0.01; ****P < 0.0001. (C) Heatmap cluster analysis of averaged SL species as in A and B. Log₁₀-transformed data with Euclidean distance measure were plotted using MetaboAnalyst Suite 5.0.

in mutant-expressing cells (Supplemental Figure 4C). The relative increase in the intermediate chain length C₁₈, C_{20:0}, and C₂₂ species in mutant-expressing cells was accompanied by a decrease in the relative proportion of abundant C_{16:0} and C_{24:0} species (Supplemental Figure 4C). An increase in the intermediate acyl chain-containing ceramides (C₁₈ to C₂₂) was also seen in primary fibroblasts isolated from L39del and F40S41del patients (Supplemental Figure 5, A and B) in which targeted siRNA-mediated knockdown of the mutant

alleles normalized the acyl chain profiles (Supplemental Figure 5C). Lastly, the plasma species profiles in patients carrying Y23F, L39del, and F40S41del showed similar changes in ceramide species (Supplemental Figure 6).

In conclusion, the lipid signature for ALS-associated variants is characterized by increased SL synthesis and accumulation of uncommon acyl chain length ceramide species, whereas in HSN1 the signature is characterized by increased deoxySL synthesis.

Serine availability modulates the clinical presentation of SPTLC1 variants. SL analysis showed clear differences between the SPTLC1 variants when expressed in cells; however, the correlation of variants with disease presentation is not always straightforward, and the L39del and S331 variants have been reported to cause both sensory and motor phenotypes (4, 25), suggesting that additional factors influence disease outcome.

L-Serine and L-alanine availability modulates the synthesis of canonical and 1-deoxy lipids, respectively, as 1-deoxySL formation is induced under conditions of L-serine restriction (26, 27). We therefore tested the effect of reduced serine availability on SL profiles of SPTLC1 variant-expressing cells. WT-SPTLC1-, ex2del-, and L39del-expressing cells were cultured at decreasing L-serine and constant L-alanine concentrations. In the absence of L-serine, we observed a reduction in total SL synthesis (Figure 5A) and an increase in 1-deoxySL synthesis in both WT- and variant-expressing cells (Figure 5B). However, the extent of 1-deoxySL formation with reduced serine conditions was higher in variant-expressing cells than in those expressing WT-SPTLC1. Interestingly, the L39del variant showed a significantly higher 1-deoxySL accumulation than the ex2del under these conditions (Figure 5B). Heatmap cluster analysis showed a gradual shift of SL enrichment profiles from the ALS lipid signature toward the HSN1 signature, which is distinguishable for the L39del mutant-expressing cells (Figure 5C).

The modulation of SL synthesis by substrate availability suggests that the concentration of L-serine and L-alanine in patients might influence the clinical presentation of SPTLC1 variants. We investigated this in the previously reported L39del family (4) where 4 children (II-1, II-2, II-3, and II-4) showed an ALS disease phenotype, and the father (I-1) presented with a sensory neuropathy that was initially diagnosed as HSN1 (Figure 6A). The difference in the clinical presentation was reflected in plasma lipid levels that revealed elevated 1-deoxySLs for the father (I-1) but not for the children (II-1, II-2, II-3, and II-4) or the unaffected mother (I-2) (Figure 6B).

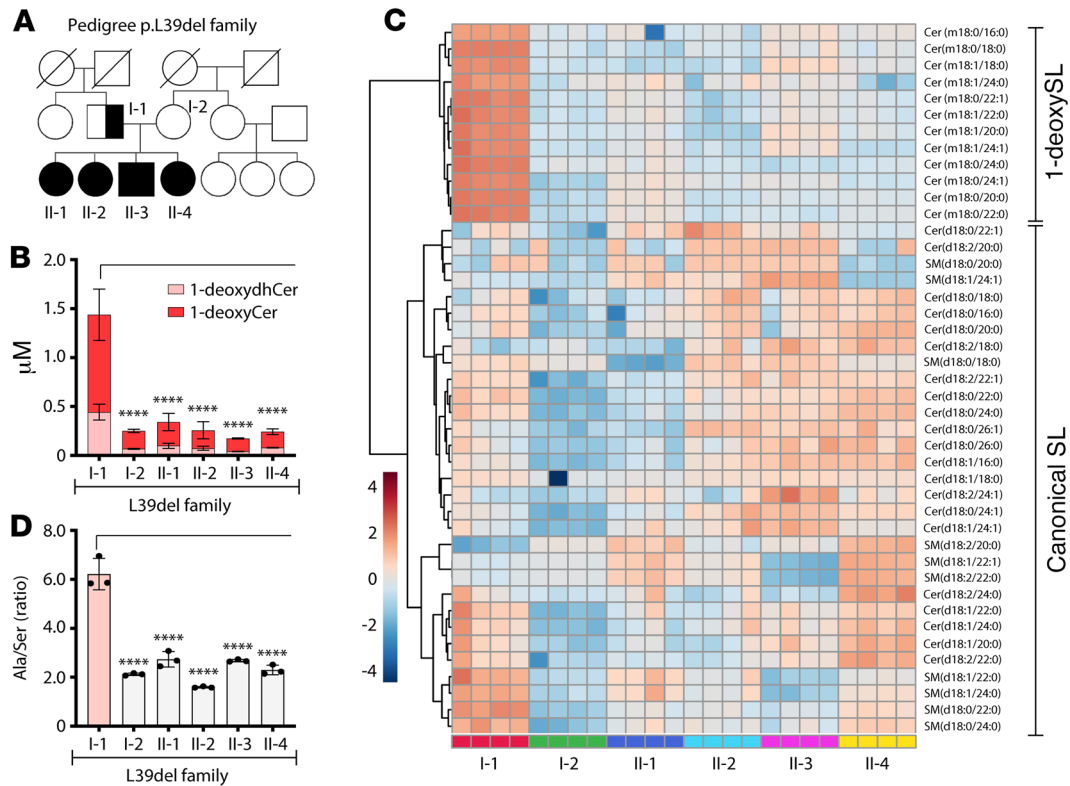


Figure 6. Sphingolipid (SL) profiles are influenced by alanine to serine ratios in vivo in the L39del family. (A) Pedigree of the family harboring the SPTLC1p.Leu39del mutation. Half-filled shapes represent a sensory phenotype, and filled shapes reflect members with motor neuron disease. Circles = females, boxes = males, I and II indicate first- and second-generation individuals. (B) Total plasma 1-deoxydihydroceramides (m18:0) (1-deoxydhCer) and 1-deoxyceramides (m18:1) in individual family members. Data are represented as mean \pm SD, $n = 4$, 2-way ANOVA with Dunnett's adjustment for multiple comparisons. (C) Heatmap cluster analysis of SL species in the plasma of the family members. Lipids were extracted and quantified from plasma independently 4 times. Log₁₀-transformed data with Euclidean distance measure were plotted using MetaboAnalyst Suite 5.0. (D) Alanine/serine ratio in the plasma of individual family members. Data are represented as mean \pm SD, $n = 3$, 1-way ANOVA with Bonferroni's adjustment for multiple comparisons. **** $P < 0.0001$.

A heatmap cluster analysis of plasma SLs within the family (Figure 6C) revealed that the lipid signature of the father resembled the pattern of HSN1 C133W-expressing cells with an additional increase in some canonical SLs (Figure 4A), but the children had a lipid signature pattern similar to cells expressing L39del or other TMD variants (Figure 4A). Since the L-serine and L-alanine concentrations are able to modulate SL and 1-deoxySL enrichment in L39del-expressing cells (Figure 5, A and B), we wanted to test whether altered amino acid balance could explain the SL differences in patients. Notably, the father showed an increased ratio of L-alanine to L-serine compared with the family members (Figure 6D), which was primarily driven by father's low plasma L-serine levels (Supplemental Figure 7A), as L-alanine levels were similar (Supplemental Figure 7B).

In summary, in addition to the genetic variations in SPTLC1, the availability of L-serine and L-alanine in patients affects the clinical phenotype and can shift the lipid signature between HSN1 and ALS.

Discussion

This study demonstrates that pathogenic variants in different domains of the SPTLC1 subunit of SPT generate distinct lipid signatures that are associated with specific clinical phenotypes. The variants associated with childhood-onset ALS cluster in the TMD, while those in the cytosolic domain are largely associated with HSN1. The pathogenic transmembrane variants do not prevent

localization to the ER, except in the case where the TMD is deleted, but they generally impair binding of the negative regulator ORMDLs to the holoenzyme complex, resulting in increased SL synthesis and distinct lipid signatures.

The SPTLC1-ALS variants in the TMD—ex2del, F40S41del, and L39del—showed the least interaction with ORMDLs (Figure 2, A and C) and, together with the adjacent L38R variant, showed impaired feedback inhibition by C₆-Cer (Figure 2F), causing a large increase in SL synthesis (Figure 3), similar to cells in which all ORMDLs were silenced (Figure 2, D and E). The ex2del variant showed the highest SL synthesis despite its mislocalization and reduced interaction with SPTLC2, highlighting the importance of the SPTLC1 TMD in regulating SPT activity. In contrast, Y23F retained the interaction with ORMDLs, and together with A20S only caused a modest increase in SL levels, suggesting that changes in the luminal residues of the TMD (Supplemental Figure 1B) are better tolerated. Additional ORMDL-independent homeostatic control points in the pathway acting downstream of SPT could exist that are not affected by the variants.

We observed differences in the saturation of sphingoid backbones (Figure 3) and the conjugated N-acyl chains (Figure 4 and Supplemental Figures 4–6) of SL species formed by the variants. These differences are not easily explained by an increased SPT activity, as most of these modifications occur downstream of SPT. N-acylation of the sphingoid backbone is determined by CERS enzymes (28),

while the double bonds in the SL backbones are introduced by the desaturases DEGS1 and FADS3 (Supplemental Figure 1A) (29, 30). In the SPTLC1-ALS-expressing cells and patient-derived fibroblasts, the relative increase was the highest for SLs conjugated to C_{18:0}, C_{20:0} and C_{22:0} acyl chains, which are usually minor species and barely detected in control cells (Figure 4, Supplemental Figure 4, A-C, and Supplemental Figure 5). A possible explanation, at least for the largely cytosolic ex2del variant, could be the distinct intracellular localization of the variant, which might alter local concentration of the metabolic intermediates, thereby also influencing the reaction kinetics of enzymes downstream in the pathway. In any case, these intermediate chain length species were specifically increased in SPTLC1-ALS and could serve as potential biomarkers for this rare condition (Supplemental Figure 6) but might also be an underlying cause for the specific motor neuron toxicity in SPTLC1-ALS.

The SPTLC1-ALS variants do not typically form 1-deoxySLs, which are the hallmark for the SPTLC1-HSAN1 variants. The A20S variant was previously shown to mediate 1-deoxySL formation *in vitro* (6); however, these results were not confirmed in our cell-based assays and under these conditions (Figure 3, G and H). The SPTLC1-HSAN1 variants S331F and S331Y showed a mixed SL phenotype that was characterized by both an increased canonical activity and a significant formation of 1-deoxySLs (Figure 3, A-H). This mixed metabolic pattern is mirrored by the clinical presentation of the HSAN1 patients having both sensory and motor symptoms (25, 31-33). Initially, the disease phenotype in the patients was characterized as hereditary motor and sensory neuropathy but the diagnosis was revised to HSAN1 when the sensory symptoms became manifest. Structural studies showed the interaction of S331 with the N-terminal ORMDL loop (16), and S331 is required for interaction with ORMDLs and for feedback inhibition by ceramides (Figure 2, A, C, and H), explaining the increased SL accumulation. Surprisingly, the HSAN1 variant C133W also showed reduced association with ORMDLs, although the feedback inhibition by C₆-Cer or synthesis of canonical SLs was similar to WT (Figure 2, A, C, and H), indicating that mechanisms other than the binding of ORMDL proteins to the holoenzyme complex may be important in regulating SPT activity.

A heatmap cluster analysis of cells expressing the SPTLC1-ALS and -HSAN1 variants showed a continuous shift in the lipid signature from the SPTLC1-HSAN1 to the SPTLC1-ALS variants (Figure 4A). On one end of the spectrum is the HSAN1 C133W variant that is associated with sensory symptoms and increased 1-deoxySLs, whereas at the other end the exon2del variant is associated with a motor neuron disease and increase in canonical SLs. This pattern suggests that the increased formation of canonical SLs with uncommon N-acyl chains is primarily toxic for the cerebral motor neurons, whereas increased 1-deoxySLs primarily affects peripheral sensory neurons. What renders these neuronal populations more susceptible to one or the other SL metabolite remains unknown.

SPTLC1-ALS variants are capable of forming significant amounts of deoxySL in conditions of L-serine deficiency (Figure 5B), and the comparison of the metabolic signatures showed that L-serine deficiency renders the SL pattern in the SPTLC1-ALS-expressing cells similar to that of the SPTLC1-HSAN1-expressing cells (Figure 5C). This raises the possibility that the motor phenotype in ALS might be converted to a more HSAN1-like phenotype through changes in amino acid availability, a hypothesis

that we investigated in the previously reported SPTLC1 L39del family (Figure 6A). Although all affected family members were carriers of the L39del variant, the index patient (I-1) showed an HSAN1 plus motor neuropathy phenotype, with elevated plasma 1-deoxySLs and a higher alanine to serine ratio due to low plasma serine levels (Figure 6, B-D, and Supplemental Figure 7A) compared with the other family members with pure motor neuron disease without sensory neuropathy. It is currently unclear why the L-serine levels were low in the index case, but it demonstrates that the two disease phenotypes are modifiable by the L-serine/L-alanine ratio. In that respect, the HSAN1 and ALS phenotypes reflect the opposite ends of a spectrum characterized by a variable degree of sensory and motor symptoms that depend on the underlying pattern of increased 1-deoxySL versus canonical SL. This has therapeutic consequences, as supplementing L-serine in HSAN1 patients should suppress 1-deoxySL formation and slow disease progression, whereas L-serine supplementation in SPTLC1-ALS patients might worsen the phenotype by stimulating the synthesis of canonical SLs.

Methods

Cell culture. Cell lines were grown in high-glucose DMEM (Wisent 319-027-CL for interaction analysis and protein biochemistry or Sigma-Aldrich D5796 for lipidomics) supplemented with 10% fetal bovine serum (FBS) in a 5% CO₂ incubator at 37°C. Cell lines were regularly tested for mycoplasma contamination. For immunofluorescence analysis, cells were cultured on glass coverslips.

Cell lines. For protein analysis, Flp-In T-Rex 293 cells (Invitrogen) were used for expressing FLAG-tagged SPTLC1 variants for the analysis of protein interactions on SDS-PAGE and native PAGE. The generation of the HEK293 SPTLC1-KO cell line (for lipidomics) was previously reported (4). SPTLC1-KO and SPTLC2-KO Flp-In T-Rex 293 cell lines (protein analysis) were reported previously (15). Patient fibroblasts were cultured in DMEM with 10% FBS as reported previously (4).

Generation of cell lines. To express FLAG-tagged SPTLC1 and pathogenic variants in SPTLC1-KO cells, cells were rescued by integration of tetracycline-inducible SPTLC1^{FLAG} in pDEST-pcDNA5 plasmids as described previously (34). Protein expression was induced with 1 µg/mL tetracycline for 4 hours. Plasmid transfections were performed with Lipofectamine 3000 (Thermo Fisher Scientific) in HEK293 SPTLC1-KO cells. Transgenic HEK293 cell lines were selected for growth in DMEM containing 400 µg/mL Geneticin (Thermo Fischer Scientific) and 1% penicillin/streptomycin (P/S).

For blue-native PAGE (BN-PAGE) analysis, control and patient fibroblasts were immortalized by transduction with retroviral vectors expressing the HPV-16 E7 gene and the catalytic component of human telomerase, as described previously (35).

Plasmids. The pcDNA5-pDEST-SPTLC1^{FLAG} plasmid was generated by flipping SPTLC1 from the pDONR221 donor vector into the pcDNA5-pDEST-3xFLAG destination vector (15) using Gateway cloning technology, yielding SPTLC1 with a C-terminal triple FLAG-tag. SPTLC1 variants were generated using mutagenesis PCR (QuikChange Lightning, Agilent) in pDONR221-SPTLC1 and flipped into the pcDNA5-pDEST-3xFLAG destination vector. The ER-mCherry (mCh-Sec61 beta) plasmid was a gift from Gia Voeltz (Addgene, 49155) (36).

For lipid analysis, SPTLC1 was cloned into the pcDNA3.1-V5-His vector. PCR-based site-directed mutagenesis was used to introduce SPTLC1-ALS and -HSAN1 mutations in the plasmid vector backbone (4, 14, 21).

Confocal microscopy. For confocal microscopy, COS-7 cells were transfected using Lipofectamine 3000 with the indicated pcDNA5-SPTLC1-FLAG and ER-marker plasmids, fixed the day after with 6% formaldehyde in PBS, solubilized with 0.1% Triton X-100 in PBS for 15 minutes at room temperature, and blocked with 5% (w/v) BSA in PBS. Primary and secondary antibodies were diluted in 5% (wt/vol) BSA in PBS, and coverslips were incubated with the antibodies for 1 hour at room temperature with 5 washes with PBS in between. Image acquisition (z -stacks, step size 0.2 μm) was performed with an Olympus IX83 confocal microscope containing a spinning disk system (Andor/Yokogawa CSU-X) using Olympus UPLSAPO 100 \times oil objectives. Images were processed in Fiji.

Membrane isolation. For separation of membrane and cytosolic fractions, cells were resuspended in fractionation buffer (20 mM HEPES-KOH pH 7.6, 1 mM EDTA, and 1 \times cOmplete protease inhibitor [Roche, 11873580001]), lysed by passing through a 25 G needle 10 times, and unbroken cells were pelleted 5 minutes at 800g 3 times. Protein concentration in lysates was determined by Bradford assay, diluted to 1 $\mu\text{g}/\mu\text{L}$, and input sample was collected and mixed with Laemmli buffer. To pellet membranes, 100 μg of lysates was centrifuged 90 minutes at 100,000g in TLA100 rotor, and soluble fractions were collected in the supernatant and mixed with Laemmli buffer. Membrane pellets were solubilized in Laemmli buffer and equal amounts of each fraction were analyzed by SDS-PAGE and immunoblotting.

For preparation of 20,000g membrane fractions for coimmunoprecipitation and BN-PAGE analysis, cells were resuspended in isolation buffer (220 mM mannitol, 70 mM sucrose, 20 mM HEPES-KOH pH 7.6, 1 mM EDTA, 1 \times cOmplete protease inhibitor) and homogenized with 15–20 strokes in a rotating Teflon-glass homogenizer at 1000 rpm. Homogenates were centrifuged twice at 800g for 5 minutes to remove nuclei and cell debris. Membranes were pelleted at 20,000g for 30 minutes, resuspended in isolation buffer, and protein concentration was determined by Bradford assay.

Denaturing and native PAGE. For analysis of protein levels in whole-cell lysates, cells were lysed with RIPA lysis buffer (1% Triton X-100, 0.1% [w/v] SDS, 0.5% [w/v] sodium deoxycholate, 1 mM EDTA, 50 mM Tris pH 7.4, 150 mM NaCl, 1 \times cOmplete protease inhibitor) for 20 minutes and centrifuged for 15 minutes at 20,000g. Equal amounts of protein were analyzed on a 10% Tris-Tricine SDS-PAGE system (37) with Precision Plus Protein standard (Bio-Rad, 1610363) as a molecular weight marker, and blotted onto a nitrocellulose membrane. Protein intensities were quantified in Fiji.

For analysis of SPT complexes on BN-PAGE, 20,000g membrane fractions were solubilized with 4 g digitonin/g protein (1% wt/vol) for 20 minutes, centrifuged for 20 minutes at 20,000g, and equal amounts of supernatants were separated in a 4%–13% gradient gel as previously described (38) with an Amersham HMW native marker kit (Cytiva, 17044501) as a molecular weight marker, and blotted onto a PVDF membrane. For SDS-PAGE analysis of protein levels in native samples, equal amounts of supernatants were mixed with Laemmli buffer and run in SDS-PAGE gel as described above.

FLAG immunoprecipitation. Membrane fractions were solubilized in buffer (50 mM Tris pH 7.4, 150 mM NaCl, 20 mM MgCl_2 , 4 g digitonin/g protein [1% wt/vol], 1 \times cOmplete protease inhibitor) for 20 minutes and aggregates were pelleted at 20,000g for 20 minutes. Input sample was taken from the supernatant and the rest was incubated with anti-FLAG magnetic M2 beads (Sigma-Aldrich, M8823) for 3 hours. Beads were washed 4 times with wash buffer (50 mM Tris pH

7.4, 150 mM NaCl, 20 mM MgCl_2 , 0.1% wt/vol digitonin, 1 \times cOmplete protease inhibitor). Samples were eluted with Laemmli buffer and analyzed by immunoblotting.

Antibodies. The following antibodies were used: anti-SPTLC1 (Sigma-Aldrich, HPA063907), anti-SPTLC2 (Abcam, ab236900), polyclonal anti-ORMDL3 (MilliporeSigma, ABN417) that detects ORMDL1, -2, and -3 (22), mouse anti-FLAG (immunofluorescence; Sigma-Aldrich, F1804), rabbit anti-FLAG (immunoblot; Proteintech, 20543-1-AP), anti-VAPB (Proteintech, 14477-1-AP), anti-UBB (Cell Signaling Technology, 3933), anti- β -actin (GenScript, A00702), anti-TOMM40 (Proteintech, 18409-1-AP), anti-HSPA5/BiP (Abcam, ab21685); and the secondary antibodies anti-mouse-Alexa Fluor 488 (Invitrogen, A-11029), anti-mouse-HRP (Jackson ImmunoResearch, 115-035-146), and anti-rabbit-HRP (Jackson ImmunoResearch, 111-035-003).

Silencing of ORMDL and SPTLC1-ALS variants. siRNAs targeting human ORMDL1, -2, and -3 (39) were used to silence ORMDL expression. The allele-specific silencing of the mutants L39del and F40S41del was based on a previously reported siRNA approach (4). For HEK293 cells, 10 nM of each siRNA was cotransfected, and for fibroblasts, 10 nM of the variant-targeting siRNA was transfected. The siRNAs were diluted in reduced-serum media (Opti-MEM; Gibco, 31985-047). Transfection was performed using Lipofectamine RNAiMAX Transfection Reagent (Thermo Fisher Scientific, 13778030) according to the manufacturer's instructions. The media were replaced after 4 hours with fresh growth media (DMEM/10% FBS) and cells were allowed to grow for 72 hours before the labeling experiments.

Stable isotope labeling assay in cells. SL labeling assays and SPT activity measurements were performed in vivo in cells. SPTLC1-KO cells expressing SPTLC1-ALS and -HSAN1 variants were plated at 200,000 cells/mL in 6-well plates. Cells were grown for 48 hours to 70% confluence in DMEM/10% FBS growth media. For standard labeling assay, the medium was replaced with L-serine-free DMEM (Genaxxon Bioscience) containing 10% FBS, 1% P/S, and D_3 - ^{15}N -L-serine (1 mM unless indicated otherwise) and 2 mM D_4 -L-alanine (Cambridge Isotope Laboratories). Cells were grown further in the labeling media for 16 hours. C_6 -Cer, when used in activity assays, was added together with the labeling media. For siRNA-mediated knockdown in HEK293 cells and fibroblasts, the assay was started 72 hours after transfection. For lipid analysis, HEK293 cells were harvested in ice-cold PBS. Fibroblasts were harvested by trypsinization (500 μL). Finally, 50 μL of cells were counted (Z2 Coulter Counter, Beckman Coulter) and cell pellets were frozen at -20°C until extraction.

Amino acid analysis. Amino acids were quantified from 10 μL plasma precipitated with 180 μL ice-cold methanol containing 1 nmol of stable isotope-labeled amino acids (Cambridge Isotope Laboratories, MSK-A2-1.2). Samples were incubated at -20°C for 30 minutes followed by centrifugation at 4°C (14,000g, 10 minutes). The supernatant was transferred to a fresh tube and dried under a N_2 stream, and stored at -20°C until analysis. Dried pellets were reconstituted in 100 μL of 0.1% acetic acid. The dissolved material was transferred to an autosampler vial following centrifugation at room temperature (16,000g, 5 minutes). Amino acids were separated on a reverse-phase C18 column (EC 250/2 NUCLEOSIL 100-3 C18HD, length 250 mm, internal diameter 2 mm; Macherey-Nagel). Samples (5 μL) were analyzed by liquid chromatography coupled with multiple reaction monitoring (MRM) mass spectrometry using a QTRAP 6500+ LC-MS/MS-MS System (SCIEX). Solvent systems used were 0.1% formic acid in water (A) and 100% acetonitrile (B). The amino acids were chromatographed isocratically with

solvent A for 5 minutes, followed by a linear gradient to 50% solvent B over 2 minutes. Then, the column was washed with 80% solvent B prior to equilibration with 100% solvent A. The flow rate was held constant at 0.2 mL/min. Sample ionization was achieved via electrospray ionization in positive ion mode. Quantification was performed using MultiQuant (2.1) software (SCIEX).

Sphingolipidomics. Frozen cell pellets were resuspended in 50 μ L PBS and extracted with 1 mL methanol/methyl *tert*-butyl ether/chloroform (4:3:3) containing 100 pmol each of D₇-sphinganine (d18:0), D₇-sphingosine (d18:1), dihydroceramide (d18:0/12:0), ceramide (d18:1/12:0), glucosylceramide (d18:1/8:0), SM (d18:1/18:1[D₉]), and D₇-sphingosine-1-phosphate. Lipids were extracted continuously using a Thermomixer (Eppendorf) at 37°C (1400 rpm, 60 minutes). The single-phase supernatant was collected, dried under N₂, and dissolved in 100 μ L methanol. Untargeted lipid analysis was performed on a high-resolution Q-Exactive MS analyser (Thermo Fisher Scientific) after lipids were separated by liquid chromatography carried out according to Taylor et al. (2) with some modifications. Lipids were separated using a C30 Accucore LC column (150 mm \times 2.1 mm, 2.6 μ m particle size) and a Transcend UHPLC pump (Thermo Fisher Scientific). Liquid chromatography was performed with acetonitrile/water (6:4) with 10 mM ammonium acetate and 0.1% formic acid (A) and isopropanol/acetonitrile (9:1) with 10 mM ammonium acetate and 0.1% formic acid (B) at a flow rate of 0.260 mL/min. The following gradient was applied: (a) 70% A/30% B, 0.0 to 0.5 minutes; (b) 57% A/43% B, 0.5 to 2.0 minutes; (c) 45% A/55% B, 2.0 to 3.30 minutes; (d) 25% A/75% B, 3.30 to 12.0 minutes; (e) 100% B, 12.0 to 25.0 minutes; (f) 70% A/30% B, 25.00 to 29.50 minutes. Lipids were similarly extracted and quantified from 50 μ L patient or control plasma. MS2 fragmentation was based on data-dependent acquisition. Lipid identification criteria were: (a) resolution with an accuracy of 5 ppm from the predicted mass at a resolving power of 70,000 at 200 *m/z*, (b) isotopic distribution, (c) fragmentation pattern, and (d) expected retention time relative to internal and external standards. Similar criteria were applied to isotope-labeled de novo-produced SLs in cells carrying an additional +3 Da.

Transitions used for labeled and nonlabeled lipids were (a) ceramide: [M+H]⁺ \rightarrow [M+H - H₂O]⁺, [M+H - 2H₂O]⁺, [M+H - H₂O - FA]⁺, and [M+H - 2H₂O - FA]⁺; (b) 1-deoxyceramide: [M+H]⁺ \rightarrow [M+H - H₂O]⁺ and [M+H - H₂O - FA]⁺; (c) hexosylceramide: [M+H]⁺ \rightarrow [M+H - H₂O]⁺, [M+H - 2H₂O]⁺, [M+H - H₂O - FA - Hex]⁺, [M+H - 2H₂O - FA - Hex]⁺; (d) SM: [M+H]⁺ \rightarrow [M+H - H₂O]⁺, [M+H - 2H₂O]⁺, [M+H - H₂O - FA - PO₄-choline]⁺, [M+H - 2H₂O - FA - PO₄-choline]⁺; (e) sphingoid base (d18:1, d18:0): [M+H]⁺ \rightarrow [M+H - H₂O]⁺ and [M+H - H₂O - H₂O]⁺; and

(f) 1-deoxysphingoid base (m18:1, m18:0): [M+H]⁺ \rightarrow [M+H - H₂O]⁺; where Hex is a hexose sugar, PO₄-choline is the phosphocholine head group, and FA is fatty acid.

Data availability statement. This study did not generate any new code. The raw data that support the findings of this study are available from the corresponding authors upon request.

Statistics. If not indicated differently, data were compared by 1-way ANOVA with Bonferroni's adjustment for multiple comparisons. Plasma SL (Supplemental Figure 3) and 1-deoxySL (Figure 6B) were compared using 2-way ANOVA with Dunnett's adjustment for multiple comparisons. All results are expressed as mean \pm standard deviation (SD). An adjusted *P* value of less than 0.05 was considered statistically significant. Statistical analyses were performed with Prism 8.0 (GraphPad Software, Inc.) and MetaboAnalyst v5.0 (www.metaboanalyst.ca) (40).

Study approval. Ethical approval for human research studies described in this paper was obtained from the following relevant institutional review boards: NIH/NINDS (protocol no. 12-N-0095), Washington University (protocol no. 201308083), McMaster University (protocol no. REB 14-595-T), and University of Massachusetts (protocol no. 13788_10).

Author contributions

MAL, MJA, EAS, and TH conceptualized the study. MAL, MJA, and SM performed experiments and analyzed the data. MAL, MJA, EAS, and TH interpreted the data. AZ, HFP, JAMS, PM, and CGB provided plasma, cells, and targeted siRNA. MAL, MJA, EAS, and TH wrote and reviewed the manuscript. All authors reviewed and approved the manuscript.

Acknowledgments

We are grateful to the patients and their families. This research was supported in part by a grant from the Canadian Institute of Health Research (173437 to EAS), the Swiss National Science Foundation (SNF 31003A_179371 to TH), the European Joint Program on Rare Diseases (EJP RD+SNF 32ER30_187505 to TH), and the Foundation Suisse de recherche sur le maladies musculaires (FSRMM to MAL).

Address correspondence to: Thorsten Hornemann, Institute of Clinical Chemistry, University Hospital Zurich, University of Zurich, Wagistrasse 14, Schlieren-8952, Switzerland. Email: Thorsten.hornemann@usz.ch; Phone: 0041.43.253.3101. Or to: Eric A. Shoubridge, Montreal Neurological Institute, McGill University, 3801 Rue University, Rm 676, Montreal, Quebec, Canada H3A 2B4. Email: eric.shoubridge@mcgill.ca; Phone: 1.514.398.1997.

- Hardiman O, et al. Amyotrophic lateral sclerosis. *Nat Rev Dis Primers*. 2017;3:17085.
- Karsai G, et al. DEGS1-associated aberrant sphingolipid metabolism impairs nervous system function in humans. *J Clin Invest*. 2019;129(3):1229-1239.
- Calvo AC, et al. Amyotrophic lateral sclerosis: a focus on disease progression. *Biomed Res Int*. 2014;2014:925101.
- Mohassel P, et al. Childhood amyotrophic lateral sclerosis caused by excess sphingolipid synthesis. *Nat Med*. 2021;27(1):1197-1204.
- Lone MA, et al. SPTLC1 p.Leu38Arg, a novel mutation associated with childhood ALS [preprint]. <https://doi.org/10.1101/2022.02.07.22269609>. Posted on medRxiv February 08, 2022.
- Johnson JO, et al. Association of variants in the SPTLC1 gene with juvenile amyotrophic lateral sclerosis. *JAMA Neurol*. 2021;78(10):1236-1248.
- Lone MA, et al. 1-Deoxysphingolipids. *Biochim Biophys Acta Mol Cell Biol Lipids*. 2019;1864(4):512-521.
- Eichler FS, et al. Overexpression of the wild-type SPT1 subunit lowers deoxysphingolipid levels and rescues the phenotype of HSN1. *J Neurosci*. 2009;29(46):14646-14651.
- Penno A, et al. Hereditary sensory neuropathy type 1 is caused by the accumulation of two neurotoxic sphingolipids. *J Biol Chem*. 2010;285(15):11178-11187.
- Houlden H, et al. Clinical, pathological and genetic characterization of hereditary sensory and autonomic neuropathy type 1 (HSAN I). *Brain*. 2006;129(pt 2):411-425.
- Auer-Grumbach M. Hereditary sensory and autonomic neuropathies. *Handb Clin Neurol*. 2013;115:893-906.
- Bejaoui K, et al. SPTLC1 is mutated in hereditary sensory neuropathy, type 1. *Nat Genet*. 2001;27(3):261-262.
- Dawkins JL, et al. Mutations in SPTLC1, encoding serine palmitoyltransferase, long chain base subunit-1, cause hereditary sensory neuropathy type 1. *Nat Genet*. 2001;27(3):309-312.
- Bode H, et al. HSN1 mutations in serine palmitoyltransferase reveal a close structure-function-phenotype relationship. *Hum Mol Genet*.

- 2016;25(5):853–865.
15. Aaltonen MJ, et al. Serine palmitoyltransferase assembles at ER-mitochondria contact sites. *Life Sci Alliance*. 2022;5(2):e202101278.
 16. Wang Y, et al. Structural insights into the regulation of human serine palmitoyltransferase complexes. *Nat Struct Mol Biol*. 2021;28(3):240–248.
 17. Li S, et al. Structural insights into the assembly and substrate selectivity of human SPT-ORMDL3 complex. *Nat Struct Mol Biol*. 2021;28(3):249–257.
 18. Han G, et al. The ORMs interact with transmembrane domain 1 of Lcb1 and regulate serine palmitoyltransferase oligomerization, activity and localization. *Biochim Biophys Acta Mol Cell Biol Lipids*. 2019;1864(3):245–259.
 19. Breslow DK, et al. Orm family proteins mediate sphingolipid homeostasis. *Nature*. 2010;463(7284):1048–1053.
 20. Han S, et al. Orm1 and Orm2 are conserved endoplasmic reticulum membrane proteins regulating lipid homeostasis and protein quality control. *Proc Natl Acad Sci U S A*. 2010;107(13):5851–5856.
 21. Lone MA, et al. Subunit composition of the mammalian serine-palmitoyltransferase defines the spectrum of straight and methyl-branched long-chain bases. *Proc Natl Acad Sci U S A*. 2020;117(27):15591–15598.
 22. Green CD, et al. CRISPR/Cas9 deletion of ORMDLs reveals complexity in sphingolipid metabolism. *J Lipid Res*. 2021;62:100082.
 23. Siow DL, Wattenberg BW. Mammalian ORMDL proteins mediate the feedback response in ceramide biosynthesis. *J Biol Chem*. 2012;287(48):40198–40204.
 24. Davis DL, et al. The ORMDL/Orm-serine palmitoyltransferase (SPT) complex is directly regulated by ceramide: reconstitution of SPT regulation in isolated membranes. *J Biol Chem*. 2019;294(13):5146–5156.
 25. Auer-Grumbach M, et al. Mutations at Ser331 in the HSN type I gene SPTLC1 are associated with a distinct syndromic phenotype. *Eur J Med Genet*. 2013;56(5):266–269.
 26. Gantner ML, et al. Serine and lipid metabolism in macular disease and peripheral neuropathy. *N Engl J Med*. 2019;381(15):1422–1433.
 27. Muthusamy T, et al. Serine restriction alters sphingolipid diversity to constrain tumour growth. *Nature*. 2020;586(7831):790–795.
 28. Hannun YA, Obeid LM. Many ceramides. *J Biol Chem*. 2011;286(32):27855–27862.
 29. Ternes P, et al. Identification and characterization of a sphingolipid delta 4-desaturase family. *J Biol Chem*. 2002;277(28):25512–25518.
 30. Karsai G, et al. FADS3 is a $\Delta 14Z$ sphingoid base desaturase that contributes to gender differences in the human plasma sphingolipidome. *J Biol Chem*. 2019;295(7):1889–1897.
 31. Rothier A, et al. Genes for hereditary sensory and autonomic neuropathies: a genotype-phenotype correlation. *Brain*. 2009;132(pt 10):2699–2711.
 32. Rothier A, et al. Characterization of two mutations in the SPTLC1 subunit of serine palmitoyltransferase associated with hereditary sensory and autonomic neuropathy type I. *Hum Mutat*. 2011;32(6):E2211–E2225.
 33. Suh BC, et al. Early-onset severe hereditary sensory and autonomic neuropathy type 1 with S331F SPTLC1 mutation. *Mol Med Rep*. 2014;9(2):481–486.
 34. Antonicka H, et al. A high-density human mitochondrial proximity interaction network. *Cell Metab*. 2020;32(3):479–497.
 35. Lochmuller H, et al. Expression of the E6 and E7 genes of human papillomavirus (HPV16) extends the life span of human myoblasts. *Exp Cell Res*. 1999;248(1):186–193.
 36. Zurek N, et al. Reticulon short hairpin transmembrane domains are used to shape ER tubules. *Traffic*. 2011;12(1):28–41.
 37. Schagger H, von Jagow G. Tricine-sodium dodecyl sulfate-polyacrylamide gel electrophoresis for the separation of proteins in the range from 1 to 100 kDa. *Anal Biochem*. 1987;166(2):368–379.
 38. Leary SC. Blue native polyacrylamide gel electrophoresis: a powerful diagnostic tool for the detection of assembly defects in the enzyme complexes of oxidative phosphorylation. *Methods Mol Biol*. 2012;837:195–206.
 39. Zhakupova A, et al. ORMDL3 expression levels have no influence on the activity of serine palmitoyltransferase. *FASEB J*. 2016;30(12):4289–4300.
 40. Chong J, et al. Using MetaboAnalyst 4.0 for comprehensive and integrative metabolomics data analysis. *Curr Protoc Bioinformatics*. 2019;68(1):e86.